Fenofibrate prevents skeletal muscle loss in mice with lung cancer

Marcus D. Goncalves[a,b,c], Seo-Kyoung Hwang[a,b], Chantal Pauli[d], Charles J. Murphy[a,b,e], Zhe Cheng[f], Benjamin D. Hopkins[a,b], David Wu[a,b], Ryan M. Loughran[a,b,1], Brooke M. Emerling[a,b,1], Guoan Zhang[f], Douglas T. Fearon[a,b,g], and Lewis C. Cantley[a,b,2]

[a]Meyer Cancer Center, Weill Cornell Medicine, New York, NY 10021; [b]Department of Medicine, Weill Cornell Medicine, New York, NY 10021; [c]Division of Endocrinology, Department of Medicine, Weill Cornell Medicine, New York, NY 10021; [d]Institute for Pathology and Molecular Pathology, University Hospital Zurich, 8091 Zurich, Switzerland; [e]Tri-Institutional Training Program in Computational Biology and Medicine, Weill Cornell Medicine, New York, NY 10021; [f]Proteomics and Metabolomics Core Facility, Weill Cornell Medicine, New York, NY 10021; and [g]CSHL Cancer Center, Cold Spring Harbor Laboratory, Cold Spring Harbor, NY 11724

Contributed by Lewis C. Cantley, December 11, 2017 (sent for review August 21, 2017; reviewed by Roy S. Herbst, Charles M. Rudin, and Paolo Sassone-Corsi)

The cancer anorexia cachexia syndrome is a systemic metabolic disorder characterized by the catabolism of stored nutrients in skeletal muscle and adipose tissue that is particularly prevalent in nonsmall cell lung cancer (NSCLC). Loss of skeletal muscle results in functional impairments and increased mortality. The aim of the present study was to characterize the changes in systemic metabolism in a genetically engineered mouse model of NSCLC. We show that a portion of these animals develop loss of skeletal muscle, loss of adipose tissue, and increased inflammatory markers mirroring the human cachexia syndrome. Using noncachexic and fasted animals as controls, we report a unique cachexia metabolite phenotype that includes the loss of peroxisome proliferator-activated receptor-α (PPARα) -dependent ketone production by the liver. In this setting, glucocorticoid levels rise and correlate with skeletal muscle degradation and hepatic markers of gluconeogenesis. Restoring ketone production using the PPARα agonist, fenofibrate, prevents the loss of skeletal muscle mass and body weight. These results demonstrate how targeting hepatic metabolism can prevent muscle wasting in lung cancer, and provide evidence for a therapeutic strategy.

cachexia | skeletal muscle | glucocorticoids | ketones | fenofibrate

The cancer anorexia cachexia syndrome (CACS) is a systemic metabolic disorder characterized by the catabolism of stored nutrients in muscle and adipose tissue. Clinically, this syndrome is characterized by loss of body weight, reduced food intake, increased markers of systemic inflammation, and progressive functional impairment (1). CACS is particularly prevalent in patients with nonsmall cell lung cancer (NSCLC), with ∼50% and 75% with early and advanced-stage disease, respectively, being affected (2, 3). These patients have increased susceptibility to chemotherapeutic toxicity, poor quality of life scores, worse response to chemotherapy, and increased mortality (4–6).

Much of the negative impact of CACS is thought to be the result of the reduction in skeletal muscle mass and, more specifically, a preferential loss of the muscle used to generate power (type II myofibers) compared with muscle used for stability (type I myofibers) (7–9). The systemic signals leading to skeletal muscle destruction in cancer are unknown; however, several mechanisms have been proposed, including tumor-released factors (10, 11), tumor-induced changes to the stromal environment (12), up-regulation of inflammatory cytokines (13–15), and hormonal dysregulation (16).

One class of hormones that plays an important role in the regulation of skeletal muscle mass during times of illness is glucocorticoids (17, 18). In patients with NSCLC, the level and circadian pattern of serum glucocorticoids are significantly altered (19–26). Glucocorticoids induce skeletal muscle degradation by enhancing the expression of genes that reduce protein synthesis and enhance protein degradation via the glucocorticoid receptor (27–30). For example, the binding of glucocorticoids to the glucocorticoid receptor leads to increased expression of *Ddit4*, which is known to reduce mammalian target of rapamycin complex 1 (mTORC1) activity (31–34), and increased expression of the E3 ligases, *Fbxo32* and *Trim63*, which bind to sarcomeric proteins and mediate breakdown of the myofibrils via the ubiquitin-proteasome system (35–39).

Therapeutic strategies that target skeletal muscle loss have been grossly unsuccessful and, despite over 60 y of investigation, there continues to be no effective treatment for CACS (40). These failures suggest that the loss of skeletal muscle mass in CACS is secondary to a more global alteration in systemic metabolism. One important confounder that limits the identification of specific signals that induce CACS is anorexia. A reduction in food intake is an important contributor to changes in body composition including skeletal muscle loss. In fact, both fasting and CACS induce a common degradation program that

Significance

The cancer anorexia cachexia syndrome (CACS) is a condition characterized by skeletal muscle degradation with no effective treatment. CACS is particularly prevalent in patients with nonsmall cell lung cancer, where it reduces quality of life and increases mortality. Using an inducible lung cancer model, we characterize the changes in intermediary metabolism that occur during CACS in mice. We identify a unique serum metabolite profile consisting of low ketones and increased glucocorticoid levels. Hypoketonemia is associated with reduced expression of hepatic peroxisome proliferator-activated receptor-α (PPARα) targets that regulate fatty acid oxidation and ketogenesis. Replacing ketone production using the PPARα agonist, fenofibrate, reduced glucocorticoid levels, prevented skeletal muscle wasting, and minimized weight loss. These exciting results provide important preclinical data toward a therapeutic strategy.

Author contributions: M.D.G., D.T.F., and L.C.C. designed research; M.D.G., S.-K.H., C.P., C.J.M., Z.C., B.D.H., D.W., R.M.L., B.M.E., and G.Z. performed research; Z.C., B.M.E., and G.Z. contributed new reagents/analytic tools; M.D.G., S.-K.H., C.P., C.J.M., and G.Z. analyzed data; and M.D.G. and L.C.C. wrote the paper.

Reviewers: R.S.H., Yale University; C.M.R., Memorial Sloan Kettering Cancer Center; and P.S.-C., University of California, Irvine.

The authors declare no conflict of interest.

Data deposition: The data reported in this paper have been deposited in the Gene Expression Omnibus (GEO) database, https://www.ncbi.nlm.nih.gov/geo (accession no. GSE107470).

[1]Present address: Cancer Metabolism and Signaling Networks Program, Sanford Burnham Prebys Medical Research Institute, La Jolla, CA 92037.

[2]To whom correspondence should be addressed. Email: lcantley@med.cornell.edu.

This article contains supporting information online at www.pnas.org/lookup/suppl/doi:10.1073/pnas.1714703115/-/DCSupplemental.

includes the aforementioned E3 ligases and the ubiquitin-proteasome system (41). Therefore, the contribution of anorexia to altered systemic metabolism must be taken into account in CACS models (42).

KRAS, *LKB1*, *EGFR*, and *TP53* are the most frequently mutated genes in human NSCLC (43). Two important risk factors for developing CACS are (*i*) the presence of a *KRAS* mutation and (*ii*) the presence and burden of metastasis (44); however, genetically engineered mice with a *Kras* mutation (G12D) alone do not promptly develop CACS or metastasis (45). When *Lkb1* deficiency is introduced to *Kras*-mutated tumors, an aggressive, metastatic phenotype arises, and we hypothesized that this combination of mutations would recapitulate the human CACS syndrome in mice (46, 47).

The aim of the present study was to assess the changes in systemic metabolism in an inducible, genetically engineered mouse model of NSCLC. We show that a portion of these animals develop the human CACS syndrome, including: loss of skeletal muscle (type II myofiber atrophy), loss of adipose tissue, decreased food intake, and increased inflammatory markers. Using tissues from noncachexic and fasted animals as controls, we report a unique CACS gene and metabolite signature that included the loss of peroxisome proliferator-activated receptor-α (PPARα) -dependent ketone production in the liver. In this setting, glucocorticoid levels rise and correlate with degradation of type II muscle fibers and markers of hepatic gluconeogenesis. This process could be stopped by restoring ketone production using the PPARα agonist, fenofibrate, which prevented weight loss and protected mice from the loss of skeletal muscle mass. These results demonstrate how targeting the hepatic metabolism can prevent muscle wasting in lung cancer.

Results

A Subset of Mice with NSCLC Develop Cachexia. Given the aggressive tumor phenotype and potential for metastasis, we hypothesized that $Kras^{G12D/+}$;$Lkb1^{f/f}$ (KL) mice would develop CACS. Tumors were induced in the lungs of adult KL mice via intranasal administration of adenovirus-containing Cre recombinase (Cre), as previously described (46). Using a clinically relevant threshold for moderate weight loss, CACS was a priori-defined as a loss of 10% or more of body weight from the peak weight obtained during the study (48). Body weight was measured weekly in a cohort of mice induced with Cre or control mice treated with an empty adenovirus vector (Empty). Sixty-percent (12 of 20) of mice treated with Cre developed CACS, while the other 40% and the Empty-treated mice maintained their body weight over the duration of the study (Fig. 1*A*). The divergence in the Cre-treated population occurred about 6 wk following treatment and was associated with a reduction in food intake compared with the Empty-treated mice (Fig. 1*B*). The loss of body weight included a reduction in skeletal muscle, as demonstrated by significant decrease in gastrocnemius mass (Fig. 1*C*), and white adipose tissue (WAT), as demonstrated by a significant decrease in the mass of the gonadal fat pad (Fig. 1*D*) compared with Empty-treated mice. Liver mass was significantly reduced in both non-CACS tumor-bearing mice and CACS compared with Empty-treated mice (Fig. 1*E*), whereas kidney mass was unchanged (Fig. 1*F*).

Cachexia Does Not Correlate with Tumor Burden or Subtype of Lung Cancer. KL mice develop aggressive, metastatic tumors with either an adenocarcinoma or squamous cell phenotype similar to human NSCLC (46, 49). To determine if CACS mice featured a predominant tumor type or a greater degree of tumor burden, we histologically examined lung tumors from non-CACS and CACS mice (Fig. 2 and Table S1). Overall, we detected several subtypes of adenocarcinoma (acinar, mucinous, and papillary) and adenocarcinoma in situ (lepidic, mucinous, and papillary), with no evidence of squamous cell carcinoma. Mice with CACS tended to have more tumor with an acinar subtype of adenocarcinoma. We observed lymph node metastasis in four mice, all of which had CACS (Fig. 2*A* and Table S1). No brain or lymph node metastasis were observed grossly. The degree of tumor burden, as measured by the percent of lung occupied by tumor, did not correlate significantly with the degree of weight loss (Fig. 2*B*).

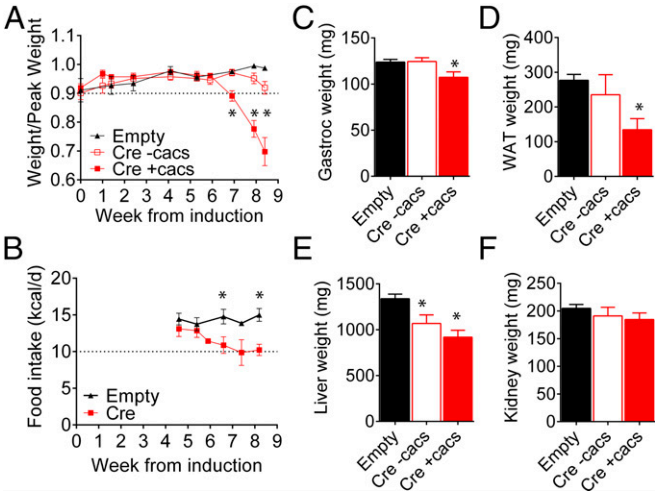

Fig. 1. Cachexia development in genetically induced lung cancer. (*A*) Weight normalized to peak weight over time following induction of lung cancer using adenovirus to deliver Cre recombinase (Cre, red boxes) and control mice treated with an empty adenovirus (Empty, black triangles, $n = 6$). Following Cre treatment, $n = 12$ mice developed cachexia (+cacs) and $n = 8$ mice maintained their weight (−cacs). (*B*) Food intake in mice from *A* treated with Empty or Cre virus. (*C*) Gastrocnemius (Gastroc) weight in Empty, Cre−cacs, and Cre+cacs mice. (*D*) Gonadal WAT weight in Empty, Cre−cacs, and Cre+cacs mice. (*E*) Liver weight in Empty, Cre −cacs, and Cre +cacs mice. (*F*) Kidney weight in Empty, Cre −cacs, and Cre +cacs mice. Bar graphs are mean ± SEM. Student's *t* test comparisons with the Empty group. $*P < 0.05$.

Cachexic Mice Have a Unique Serum Metabolite Profile Characterized by Hypoketonemia. To assess for changes in systemic metabolism that could account for CACS development, we measured serum metabolites, hormones, and cytokines involved in nutrient homeostasis in tumor-bearing mice (Fig. 3 and Fig. S1). Because of the significant overlap of shared features between CACS and anorexia, we included a cohort of nontumor-bearing fed and fasted mice. In comparison with fed mice, fasted mice had reduced serum glucose (89 ± 4 vs. 167 ± 6 mg/dL, $P < 0.001$), increased β-hydroxybutyrate (BHB) (0.69 ± 0.19 vs. 0.09 ± 0.02 mM, $P < 0.05$), and increased nonesterified fatty acids (NEFA) (1.66 ± 0.10 vs. 0.36 ± 0.05 mEq/L, $P < 0.001$), all of which are expected following fasting. There was a trend toward an increase in serum triglycerides (TG) (155.1 ± 23 vs. 101.8 ± 17.7 mg/dL, $P = 0.10$) in fasted mice. Interestingly, the most severely CACS mice (weight loss more than 15%) displayed a unique metabolic phenotype consisting of low glucose (88 ± 7 vs. 138 ± 8 mg/dL, $P < 0.001$), high NEFA (2.19 ± 0.40 vs. 1.30 ± 0.06 mEq/L, $P < 0.05$), and very low BHB (0.09 ± 0.04 vs. 0.37 ± 0.05 mM, $P < 0.01$) compared with non-CACS mice. Acetoacetate, another ketone body produced by the liver, could not be detected in the serum of any mice. Levels of serum lactate, insulin, insulin-like growth factor-1 (IGF1), and insulin-like growth factor binding protein-3 (IGFBP3) were not significantly different in CACS vs. non-CACS mice (Fig. S1). Three of the CACS mice had detectable IL-6 in the serum (~15 pg/mL), while IL-6 was not detectable in the serum of the non-CACS mice (Fig. S1). Corticosterone levels were similar between CACS and non-CACS mice until 6 wk following

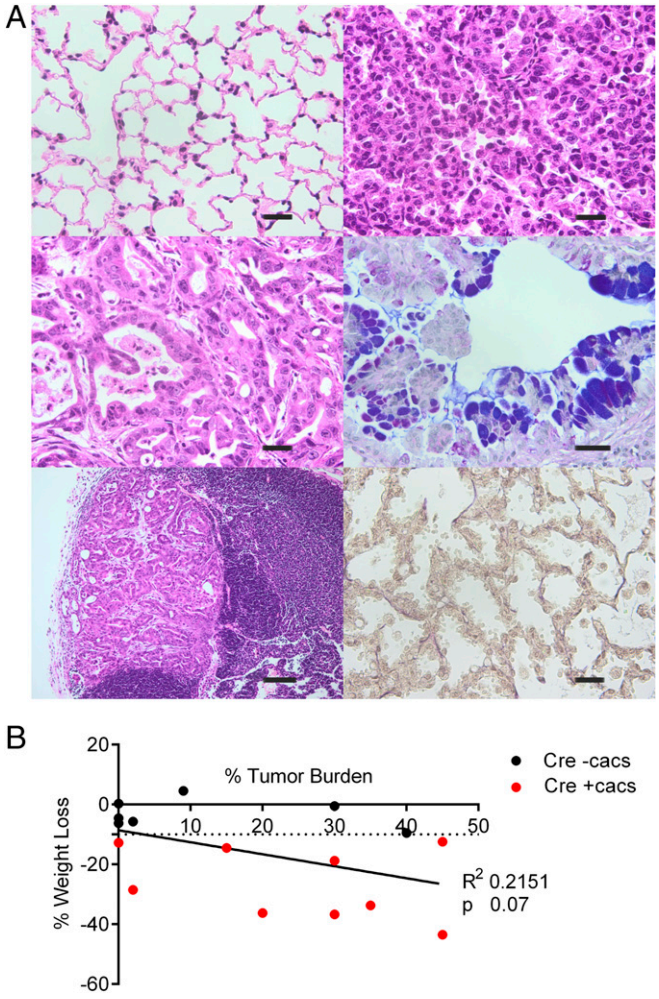

Fig. 2. Cachexia does not correlate with tumor burden or subtype of lung cancer. (*A*) Normal lung (*Top*, *Left*), adenocarcinoma subtypes identified histologically: papillary (*Top*, *Right*), acinar (*Middle*, *Left*), mucinous (*Middle*, *Right*), lymph node metastasis containing acinar adenocarcinoma (*Bottom*, *Left*), and lepidic subtype of adenocarcinoma in situ (*Bottom*, *Right*). (Scale bars: *Right Top*, *Middle*, and *Bottom* and *Left Middle*, 50 μm; *Left Top* and *Bottom*, 100 μm.) (*B*) Percent of total weight loss over the duration of the study vs. tumor burden, as defined by the percent of lung replaced by tumor in mice with (Cre +cacs, red circles) or without (Cre −cacs, black circles). Linear regression analysis (R^2, coefficient of determination, and p, *P* value).

Cre administration when the levels increased in CACS mice but not in non-CACS mice (Fig. 3*B*).

Cachexic Mice Have Reduced Hepatic Fatty Acid Oxidative Capacity and Increased Markers of Gluconeogenesis. Ketones are an important source of energy for peripheral tissues in times of carbohydrate deficiency. The liver produces ketones using the oxidation of NEFA to generate Acetyl CoA. Acetyl CoA then undergoes two condensation reactions to form β-hydroxy-β-methylglutaryl-CoA (HMG-CoA) by the enzyme, HMGCS2. HMG-CoA can then be cleaved to generate acetoacetate or cleaved and reduced to produce BHB by BDH1. Acetyl CoA is diverted away from HMGCS2 to enter the TCA cycle when sufficient oxaloacetate (OAA) is available and citrate synthase is active. Therefore, one potential cause of hypoketonemia in CACS mice could be an increase in hepatic OAA content or production.

Glycogen is a major contributor to hepatic OAA, so we measured glycogen content in the livers of fed, fasted, and tumor-bearing mice. Compared with fed mice, glycogen content was reduced in tumor-bearing and fasted mice to a similar degree (Fig. 4*A*). Because glycogen is not the sole contributor to OAA levels, we directly measured glycolytic and TCA cycle metabolites from liver tissue, including pyruvate, OAA, and citrate. Surprisingly, the relative amount of OAA in livers from CACS mice was significantly lower than non-CACS mice, thereby favoring the diversion of Acetyl CoA to ketogenesis (Fig. 4*B*). The level of citrate was similar in all groups, suggesting normal citrate synthase activity in CACS mice. Consistent with our findings from the serum, the 16 and 18 carbon saturated fatty acids, palmitate and stearate, were significantly increased in the livers of CACS mice, whereas BHB was significantly reduced in comparison with non-CACS mice. Interestingly, the abundance of BHB from the livers of fasted mice was also reduced in comparison with non-CACS mice. When measured in the gastrocnemius, however, fasted mice had a dramatic increase in BHB content, suggesting the liver rapidly secretes ketones after they are formed in the fasted state.

Another potential cause for hypoketonemia in CACS mice is a reduction in the oxidation of NEFA. AMPK can regulate fatty acid oxidation by phosphorylating and inhibiting Acetyl CoA carboxylase (ACC). Consequently, Malonyl CoA levels fall, which relieves the negative inhibition on NEFA entry into the mitochondria via CPT1. We probed hepatic liver lysates from nontumor-bearing fed and fasted mice in comparison with tumor bearing non-CACS and CACS mice for evidence of AMPK activation (Fig. S2). The level of serine 79 phosphorylation of ACC in CACS was unchanged when normalized for total ACC abundance (phospho/total) compared with non-CACS livers. Regarding AMPK itself, the phospho/total ratio of threonine 172 was significantly reduced in CACS compared with non-CACS, an effect mostly driven by a decreased amount of total AMPK in non-CACS lysates. Two other AMPK targets, Raptor and ULK1, were also altered in our samples. The phospho/total ratio of Raptor was increased in non-CACS liver lysates, whereas phosphorylation of ULK1 was unchanged. Additionally, the total protein content of both Raptor and ULK1 were significantly reduced in CACS compared with the non-CACS state.

Because of the significant differences in protein abundance between non-CACS and CACS livers, we decided to more globally assess changes in metabolism at the enzymatic level by performing RNA-Seq on livers from non-CACS, CACS, and fasted mice. At a whole-transcriptome level, mice from each group clustered together in an unbiased principal component analysis (Fig. S3*A*). A pathway enrichment analysis using the differentially expressed genes among the three groups identified the following Kyoto Encyclopedia of Genes and Genomes (KEGG) pathways as down-regulated in CACS: peroxisome, the PPAR signaling pathway, and fatty acid metabolism. We reviewed the gene expression of the β-oxidation pathway and noticed several PPARα target genes were reduced in CACS mice, including *Acox1*, the first and rate-limiting enzyme of the peroxisomal β-oxidation pathway, and the key genes involved in ketogenesis, *Hmgcs2* and *Bdh1* (Fig. S3*B*). We measured the protein products of these genes by Western blot and confirmed a reduction in *Acox1* abundance (Fig. 4 *C* and *D*). Protein levels of HMGCS2 and BDH1, however, were not decreased.

To function as a transcription factor, PPARα must translocate into the nucleus where it can associate with the transcription apparatus (50). We measured the abundance of PPARα protein in nuclear and cytoplasmic liver fractions by immunoprecipitation (Fig. 4*E* and Fig. S3 *C* and *D*). Mice without CACS displayed high levels of nuclear PPARα in comparison with fed, fasted, and fenofibrate- (a PPARα agonist) treated mice. In CACS livers, PPARα level was reduced in both the nucleus and cytoplasm in comparison with non-CACS mice.

The following KEGG pathways were up-regulated in the livers of CACS mice: ribosome, arginine biosynthesis, and glucagon

A

Cohort	% Weight Change	Glucose (mg/dL)	BHB (mM)	NEFA (mEq/L)	TG (mg/dL)
Fed		150	0.14	0.54	130.8
Fed		164	0.12	0.24	39.8
Fed		165	0.13	0.33	140.9
Fed		187	0.03	0.33	101.5
Fed		167	0.06	0.35	96.1
Fast		97	0.71	1.89	77.7
Fast		79	0.19	1.61	128.4
Fast		97	0.37	2.02	157.1
Fast		71	1.38	1.52	248.2
Fast		95	1.09	1.55	175.1
Fast		93	0.39	1.38	144.1
Cre	4.6%	155	0.34	1.21	83.5
Cre	0.3%	123	0.55	1.35	86.3
Cre	-0.5%	143	0.13	1.09	64.0
Cre	-4.6%	121	0.15	1.15	91.2
Cre	-5.7%	165	0.42	1.54	122.2
Cre	-6.2%	123	0.51	1.63	98.5
Cre	-12.4%	179	0.51	1.36	59.0
Cre	-12.8%	156	0.33	1.23	99.2
Cre	-14.5%	113	0.43	1.17	125.5
Cre	-18.8%	111	0.00	2.21	138.0
Cre	-33.7%	100	0.18	2.01	60.2
Cre	-36.2%	82	0.00	3.96	212.1
Cre	-36.7%	94	0.00	2.26	76.5
Cre	-43.5%	81	0.17	1.60	74.1

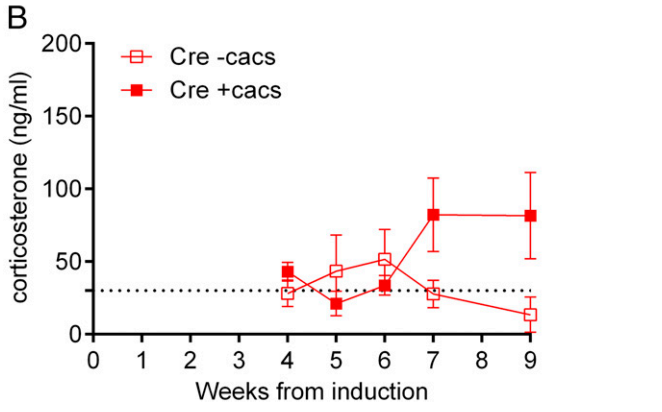

Fig. 3. Changes in serum metabolites and hormones in mice with and without cachexia. (*A*) Percent weight loss, serum glucose, BHB, NEFA, and TG in fed (Fed) and fasted (Fast) nontumor-bearing mice and tumor-bearing (Cre) mice. Values in each column are color-coded in a red (highest) to blue (lowest) heatmap. (*B*) Serum corticosterone (mean ± SEM) levels over time following induction of lung cancer in noncachexic (Cre −cacs, red open boxes, $n = 5$) and cachexic (Cre +cacs, red closed boxes, $n = 12$).

signaling pathway. We noticed that the glucagon signaling pathway contained the gene, *Pck1*, which is the major regulatory point for gluconeogenesis, so we searched our dataset for other differentially expressed genes capable of generated gluconeogenic precursors. Remarkably, many genes involved in the conversion of amino acids into pyruvate were increased in CACS livers (Fig. 4 *F* and *G* and Fig. S3*F*). This finding is in agreement with the increase in pyruvate (Fig. 4*B*) and the metabolites of upper glycolysis (Fig. S3 *G* and *H*) identified in the metabolomic analysis. All of these results suggest that PPARα-dependent fatty acid oxidation is impaired and gluconeogenesis is enhanced in the liver of CACS mice compared with non-CACS mice.

BHB is an endogenous inhibitor of histone deacetylases (HDACs) (51, 52). Therefore, some of the changes in gene expression observed in the livers of CACS mice could be explained by altered histone acetylation. We measured the level of acetylated (Lys9/Lys14) histone H3 in the livers of fed, fasted, and tumor-bearing mice and observed a significant reduction in acetylation in CACS mice (Fig. S3*E*).

Cachexic Muscle Has Reduced Type II Myofiber Size, Reduced mTORC1 Activity, and Altered Amino Acid Content. Skeletal muscle is a reservoir for amino acids that the liver can use to replete the TCA cycle and serve as gluconeogenic substrates in times of carbohydrate deficiency (53). This effect is driven by glucocorticoid-dependent degradation of type II myofibers (27, 29). Given that the CACS mice in our model have increased corticosterone levels and evidence of increased gluconeogenic capacity in the liver, we interrogated changes in skeletal muscle fiber type using the extensor digitorum longus (EDL) and the soleus as examples of type II and type I myofiber-containing muscles. EDL mass was significantly reduced in CACS mice, whereas the mass of the soleus was unchanged (Fig. 5*A*). We measured the cross sectional area (CSA) of each fiber type using antibodies against specific myosin heavy chain isoforms (Fig. 5*B*) (54). In the EDL and, to a lesser extent, the soleus, we detected a shift toward smaller myofiber CSA (Fig. 5*C*). Type I and type IIa myofibers from CACS mice were similar in size compared with non-CACS in the EDL and soleus (Fig. 5 *D* and *E*); however, the CSA of type IIx and IIb myofibers were dramatically reduced (Fig. 5*E*).

We performed RNA-Seq in the gastrocnemius muscle from non-CACS, CACS, and fasted mice to identify gene-expression patterns that would explain the loss of type IIx and IIb myofibers. Like the liver, the overall skeletal muscle expression pattern was very consistent among animals from the same condition, with striking differences between groups following unbiased clustering (Fig. 6*A*). There was a noteworthy overlap between the differentially up-regulated genes in CACS and fasted muscle (Fig. 6*B* and Dataset S1). This intersection of CACS and fasted muscle included the E3 ligases, *Fbxo32* and *Trim63*, which are known mediators of muscle breakdown in the setting of cancer and fasting (41). The genes up-regulated only in fasted muscle included the KEGG pathways: fatty acid degradation, the PPAR signaling pathway, and peroxisome. The genes specifically up-regulated in CACS muscle included the KEGG pathways: proteasome, mTOR signaling pathway, and lysosome. Specifically, the glucocorticoid-regulated mTOR inhibitor *Ddit4*, the regulatory subunit of phosphoinositide-3 kinase *Pik3r1*, and the main transcriptional target of the insulin signaling cascade, *Foxo1*, were differentially increased in only CACS muscle. We validated some of these gene-expression changes using qPCR (Fig. 6*C*).

In accordance with the changes at the level of mRNA expression, we detected significant differences in the abundance of signaling proteins in CACS skeletal muscle. The *Pik3r1* protein product, p85, was increased in comparison with non-CACS tissue (Fig. 6*D* and Fig. S4). Also, in agreement with an increased expression of *Ddit4* and *Sesn1*, phosphoprotein markers of mTORC1 and S6K activity were reduced, including phosphorylation of serine 235/6 of S6, serine 757 of ULK1, and threonine 37 of 46 of 4E-BP1. This reduction in mTORC1 activity was associated with significant differences in amino acid abundance in the gastrocnemius (Fig. 6*E*). Gluconeogenic amino acids, such as alanine and glycine, were significantly reduced in CACS compared with non-CACS muscle. Conversely, the branched chain amino acids (BCAAs) and amino acids with either basic or acidic side chains were increased. These results are consistent with a model in which glucocorticoids induce the expression of mTORC1 inhibitors, which promote muscle degradation.

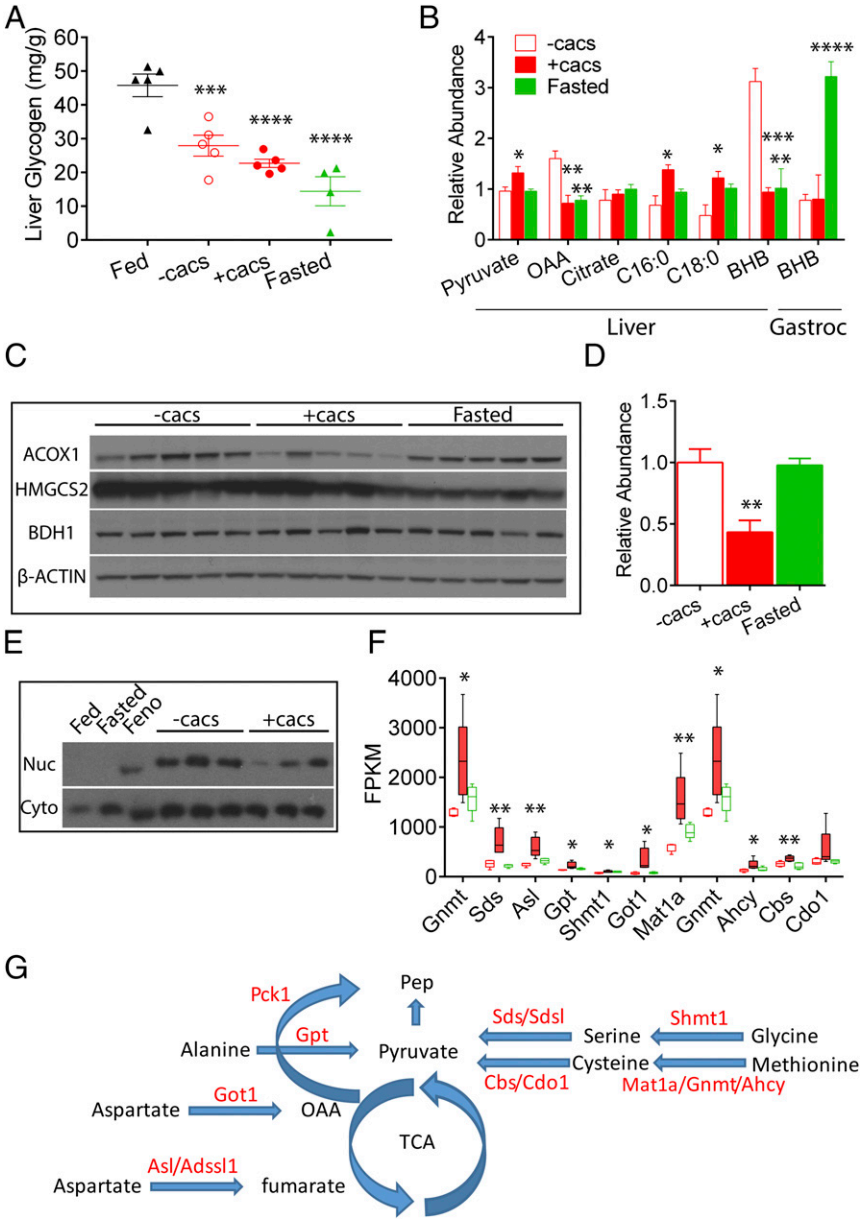

Fig. 4. Changes in liver metabolites and gene expression in fasted and tumor-bearing mice. (*A*) Liver glycogen content in fed (Fed) and fasted (Fasted) nontumor-bearing mice and tumor-bearing mice with (+cacs) and without (−cacs) cachexia. (*B*) Pyruvate, OAA, citrate, palmitate (C16:0), stearate (C18:0), and BHB metabolite abundance relative to noncacs liver and gastrocnemius (Gastroc). n = 5 each. (*C*) Immunoblot of liver lysates for indicated proteins. (*D*) Normalized quantitation of ACOX1 intensity over β-actin intensity from the immunoblot in *D* normalized to the average value from the −cacs group. (*E*) PPARα immunoprecipitation from hepatic nuclear (Nuc) and cytoplasmic (Cyto) fractions taken from Fed, Fasted, fenofibrate (Feno)-treated, and tumor-bearing mice −cacs and +cacs. (*F*) FPKM from RNA-Seq for indicated genes in −cacs, +cacs, and Fasted mice. Box and whiskers plot with minimum and maximum whiskers. (*G*) Schematic view of pyruvate generated from different amino acids using genes from *F*. Red color denotes up-regulated genes. Bar graphs are mean ± SEM. Student's t test compared with Fed mice in *A* and to −cacs in *B*, *D*, and *E*. $^{*}P < 0.05$, $^{**}P < 0.01$, $^{***}P < 0.001$, $^{****}P < 0.0001$.

The PPARα Agonist, Fenofibrate, Restores Ketogenesis and Prevents Skeletal Muscle Loss in Tumor Bearing Animals. CACS mice display a hypoketonemic phenotype that is associated with a reduction in hepatic fatty acid oxidation genes (e.g., *Acox1*) that are known to be regulated by PPARα. We hypothesized that treatment with a PPARα agonist would restore hepatic ketogenesis, prevent the reliance on hepatic gluconeogenesis, and thereby avert the need to degrade type II myofibers for amino acids. Mice were started on a 0.2% fenofibrate (Feno) diet 6 wk following the induction of NSCLC and changes in body weight and food intake were measured. Relative body weight was unchanged in mice treated with Cre compared with a cohort of nontumor bearing mice on the Feno diet (Fig. 7*A*). Food intake tended to be lower in tumor-bearing mice; however, this difference was not statistically significant (Fig. 7*B*). Tissues were harvested at 11 wk following induction and there was no difference in tumor burden in Cre treated mice on Feno compared with tumor-bearing mice on a normal chow diet.

The Feno diet induced an up-regulation in five of seven PPARα target genes we interrogated (*Hmgcs2*, *Acadm*, *Cyp4a14*, *Acox1*, *Ehhadh*, but not *Cpt1a* and *Bdh1*) in the livers of nontumor-bearing mice compared with mice on a normal chow diet (Fig. 7*C*). Tumor-bearing mice on a normal chow diet had reduced expression of *Bdh1*, *Acox1*, and *Ehhadh* compared with nontumor-bearing mice. The expression of *Hmgcs2*, *Acadm*, *Cpt1a*, *Cyp4a14*, *Acox1*, and *Ehhadh* were significantly increased in tumor-bearing mice on the Feno diet compared with Cre-treated mice on a normal chow diet. These changes in hepatic gene expression protected against the CACS serum profile we identified earlier. Serum BHB was increased in both nontumor-bearing and Cre-treated mice on Feno, and serum NEFA in Cre-treated animals was reduced to the level found in nontumor-bearing mice (Fig. 7*D*). Importantly, the restoration of ketogenesis with Feno was associated with reduced corticosterone levels (Fig. 7*E*), preserved gastrocnemius mass (Fig. 7*F*), increased liver mass, and showed a modest improvement in WAT mass (Fig. 7*G*). The mass of the EDL (which contains type IIb and IIx fibers) but not the mass of the soleus (mainly I and IIa fibers) was increased with Feno treatment in comparison with tumor-bearing mice on a normal chow (Fig. S4*A*).

We conducted a subanalysis comparing tumor-bearing mice on normal chow and Feno that lost similar amounts of weight

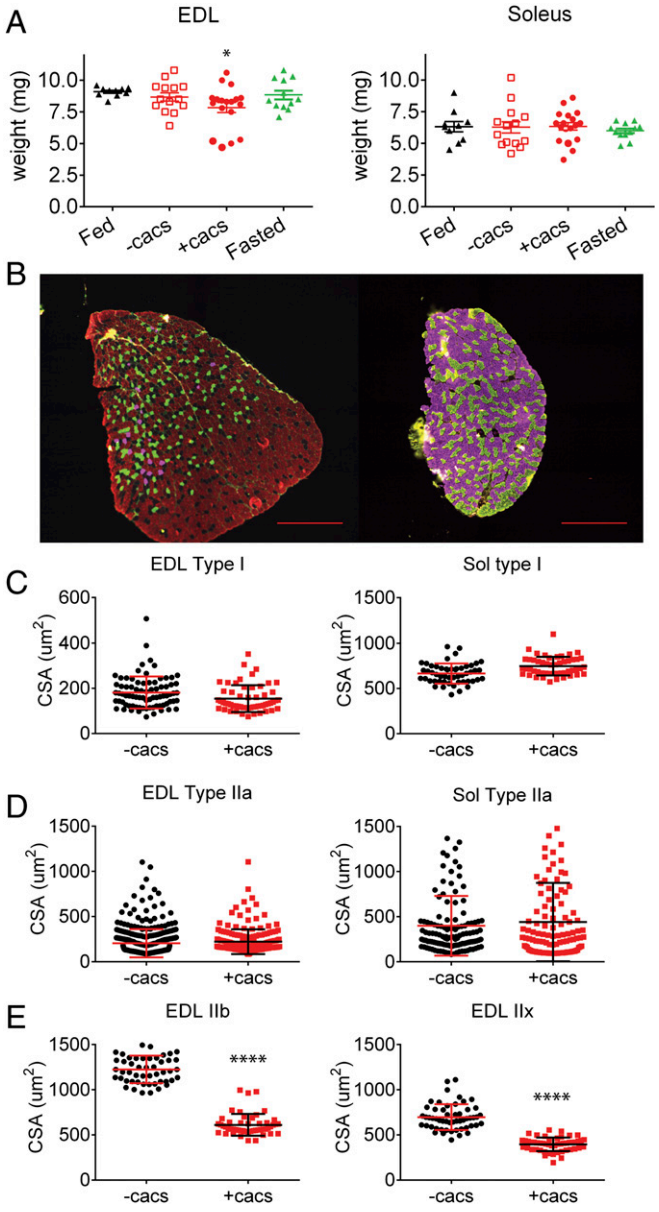

Fig. 5. Cachexia promotes Type IIx/b myofiber atrophy. (*A*) EDL and soleus muscle weight in nontumor-bearing fed and fasted mice in comparison with tumor-bearing mice with (+cacs) and without (–cacs) cachexia. (*B*) Representative photomicrograph of skeletal muscle cross-section following myosin heavy-chain fiber typing using immunofluorescence on EDL (*Left*) and soleus (*Right*). Cy5 (pink, type I), GFP (green, type IIA), unstained (black, type IIx), and dsRed (red, type IIB). (Scale bar, 320 μm.) (*C*) Type I and (*D*) type IIA myofiber CSA from noncachexic (black, –cacs) and cachexic (red, +cacs) EDL (*Left*) and soleus (*Right*) muscles. (*E*) Type IIx (*Left*) and type IIb (*Right*) EDL myofiber CSA from noncachexic (black, –cacs) and cachexic (red, +cacs) mice. Myofiber CSA from $n = 3$ mice were pooled to obtain data for *C*–*E*. Mean ± SEM indicated in each plot. Student's *t* test comparing –cacs and +cacs groups, $^{*}P < 0.05$, $^{****}P < 0.0001$.

(Fig. S4 *B*–*I*). In this analysis of primarily non-CACS mice, Feno induced a large increase in liver weight and a significant reduction in serum NEFA. Other serum metabolites (glucose, BHB) and tissue weights (gastrocnemius, WAT, and kidney) were unchanged.

Discussion

In this study we used a genetically engineered mouse model of NSCLC along with fasted animals as controls to characterize the changes in intermediary metabolism that occur with CACS. We identified a unique metabolic phenotype in CACS animals characterized by low serum glucose, increased NEFA, and reduced BHB. Using traditional biochemical assays, targeted metabolite profiling, and RNA-Seq in the liver and skeletal muscle, we have shown that the loss of serum ketones is the result of a rewired hepatic metabolism favoring gluconeogenesis and suppressing expression of PPARα target genes involved in fatty acid oxidation. This rewiring was associated with a rise in serum glucocorticoids, which degrades type II muscle fibers to provide amino acid substrate to the liver for glucose production. Treating with fenofibrate induced hepatic proliferation, restored PPARα-dependent gene expression, reversed the CACS metabolic phenotype, and prevented skeletal muscle wasting (Fig. 7*H*).

KL mice are an ideal preclinical model to study CACS. Following induction, this model accumulates significant tumor burden and lymph node metastasis in a convenient time frame. We found that 60% of tumor-bearing KL mice developed CACS. This finding is similar in magnitude to the incidence of CACS in humans with NSCLC (50–75%), but it may be an overestimate of true CACS from a metabolic point of view (2, 3). Despite our a priori definition of CACS as 10% weight loss, we only detected a distinct metabolic phenotype in tumor bearing mice that lost over 15% of peak body weight. Therefore, future studies should use this higher, experimentally determined cut-off value.

The liver is a critical regulator of whole-body glucose and lipid metabolism. In this study, we determined that CACS mice have reduced ketogenesis due to a reduction in PPARα-dependent gene expression that can be overcome using the PPARα agonist, fenofibrate. Fenofibrate modulates the expression of PPARα target genes involved in lipoprotein and fatty acid metabolism in the liver, thereby reducing the availability of NEFA for TG synthesis and export. The resulting clinical effect is a modest reduction in serum TG and TG-rich lipoproteins for which it has received Food and Drug Administration approval (55). We predict that other strategies to induce PPARα signaling would protect against muscle loss in tumor-bearing animals. For example, consumption of the n-3 polyunsaturated fatty acids, eicosapentaenoic acid and docosahexaenoic acid, induce the expression of PPARα targets genes, such as *Acox1* (56). This finding, in combination with our present results, may explain the potential benefit of omega-3 supplements in CACS (57).

Our work complements the findings of Masri et al. (58), which identified the unexpected role of lung adenocarcinoma as a potent organizer of the hepatic circadian rhythm, including changes to both gluconeogenesis and lipid metabolism. One potential contributor to these changes in gene expression is a loss of hepatic BHB, which is an endogenous inhibitor of HDACs (51, 52). The loss of BHB production is expected to increase HDAC function and reduce histone acetylation. In support of this theory, we show that CACS mice have reduced levels of histone H3 acetylation in the liver. Future studies should focus on the role of epigenetic changes, including histone acetylation at the promoters of gluconeogenic genes and PPARα targets.

In agreement with our findings, Flint et al. (59) recently identified reduced ketogenesis in both the C26 allograft CACS model and the KPC ($Kras^{G12D/+}$; $Trp53^{R172H/+}$; *Pdx-1*-Cre/+) genetically engineered mouse model of pancreatic ductal adenocarcinoma, suggesting that the hypoketonemic phenotype is important in other CACS-related cancer types. In their model, IL-6 is a necessary and sufficient upstream signal that reduces PPARα-dependent hepatic ketogenesis (59). In our study, however, the serum levels of IL-6 were only detectable in 3 of 20 tumor-bearing mice and at levels over 10-fold lower than those found in C26 or KPC mice (59), suggesting that other factors may be contributing to the suppression of PPARα. Interestingly, IL-6 can stimulate hypothalamic release of corticotropin-releasing hormone, which may drive excessive glucocorticoid production and modulate the interaction between hepatic PPARα and the glucocorticoid receptor (18).

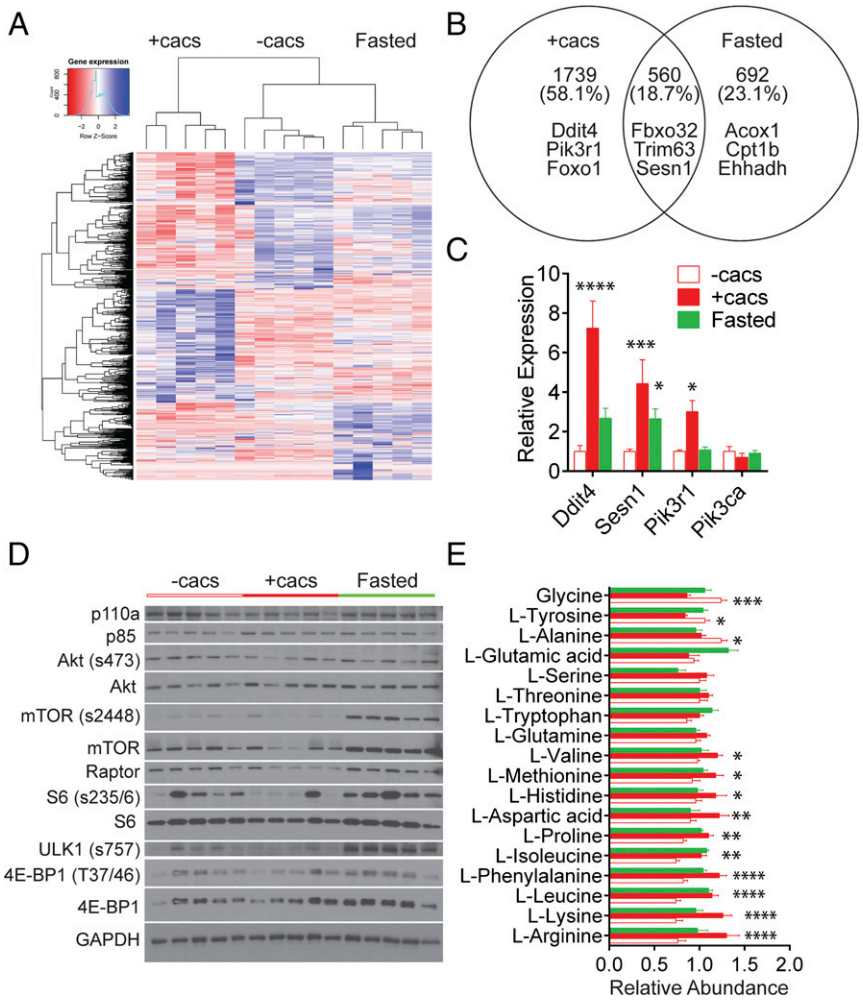

Fig. 6. Changes in skeletal muscle metabolites and gene expression in fasted and tumor-bearing mice. (*A*) Unbiased clustering of RNA-Seq using gastrocnemius from nontumor-bearing fasted mice compared with tumor-bearing cachexic (+cacs) and noncachexic (−cacs) mice. $n = 5$ each. (*B*) Venn diagram displaying the proportion and examples of differentially expressed genes in +cacs samples alone, fasted samples alone, and genes contained in both conditions. (*C*) Relative expression of −cacs, +cacs, and fasted gastrocnemius mRNA using qPCR normalized to the average value from the −cacs group. $n = 5$. (*D*) Immunoblot of tibialis anterior lysates for indicated proteins. (*E*) Relative abundance of amino acids in gastrocnemius muscles from +cacs, −cacs, and fasted mice normalized to the average value from the −cacs group. Bar graphs are mean ± SEM. Student's *t* test comparing +cacs to −cacs mice. $*P < 0.05$, $**P < 0.01$, $***P < 0.001$, $****P < 0.0001$.

The upstream regulators of PPARα in our CACS model are under active investigation. PPARα can modulate gene expression together with coactivators (e.g., PGC-1α and RXR), corepressors (e.g., NCoR1 and SMRT), or other nuclear receptors, including the glucocorticoid receptor (60). Each of these nuclear receptors can be regulated at the level of protein abundance, agonist binding, or posttranslational modifications (e.g., phosphorylation or glycosylation), which increases the complexity of the signaling network. We speculate that, in CACS, total PPARα protein level is being reduced by a posttranslational modification because the amount of *Ppara* message in the RNA-Seq analysis is not significantly different from non-CACS mice.

Our data suggest that the loss of skeletal muscle during CACS is a by-product of increased hepatic gluconeogenesis that is driven, at least in part, by glucocorticoids. This finding is in agreement with other mouse models of cancer, where glucocorticoids and gluconeogenesis are increased (12, 28, 58, 59, 61, 62), and in agreement with findings from humans with NSCLC that have changes in the level and circadian pattern of serum glucocorticoids (19–26). In our model, the rise in glucocorticoids occurred in tandem with a reduction in food intake. Interestingly, restoring serum ketones with fenofibrate treatment reduces glucocorticoid levels despite a persistent decrease in food intake. Because the hypothalamus can metabolize and respond to ketone bodies (63, 64), it is possible that the ketone bodies can directly alter the hypothalamus–pituitary–adrenal axis.

In KL mice with CACS, we found evidence of a glucocorticoid-dependent reduction in skeletal muscle protein synthesis including up-regulation of the gene, *Ddit4*, which is known to reduce mTORC1 activity (31, 32). Furthermore, we found evidence for increased expression of proteasome and lysosome genes that correlated with elevated BCAAs. BCAAs are also elevated in the serum of mice and humans with pancreatic adenocarcinoma, which is likely the consequence of glucocorticoid-dependent type II myofiber degradation (59, 65). These BCAAs can be used by the *Kras* mutant lung tumor for protein synthesis or as a source of exogenous nitrogen (66). In rodents, supplementation with BCAAs minimizes muscle loss; however, this finding is less clear in humans because of high rates of attrition during clinical trials (67). Our results support the hypothesis that lung tumors alter systemic metabolism to gain access to endogenous growth substrates, such as BCAAs.

This study quantified the metabolic alterations following the induction of lung cancer in a genetically engineered mouse model. We identified a unique combination of serum metabolites that can be used to identify animals with CACS. Using large-scale profiling techniques, we identified deficits in PPARα-dependent gene expression and showed that the PPARα activator, fenofibrate, prevents the development of CACS in mice. This protection is likely related to an enhancement in peroxisome proliferator activity in the liver resulting in improved fatty acid oxidation. These unexpected results suggest that activation of fatty acid oxidation and ketogenesis in the liver is likely to be more effective as a therapy for CACS than targeting protein metabolism in skeletal muscle.

We acknowledge that this study is limited because the results are based on a single genetically engineered mouse model and our findings need to be validated across multiple tumor types and distinct oncogenic drivers. Additionally, we are eager to confirm

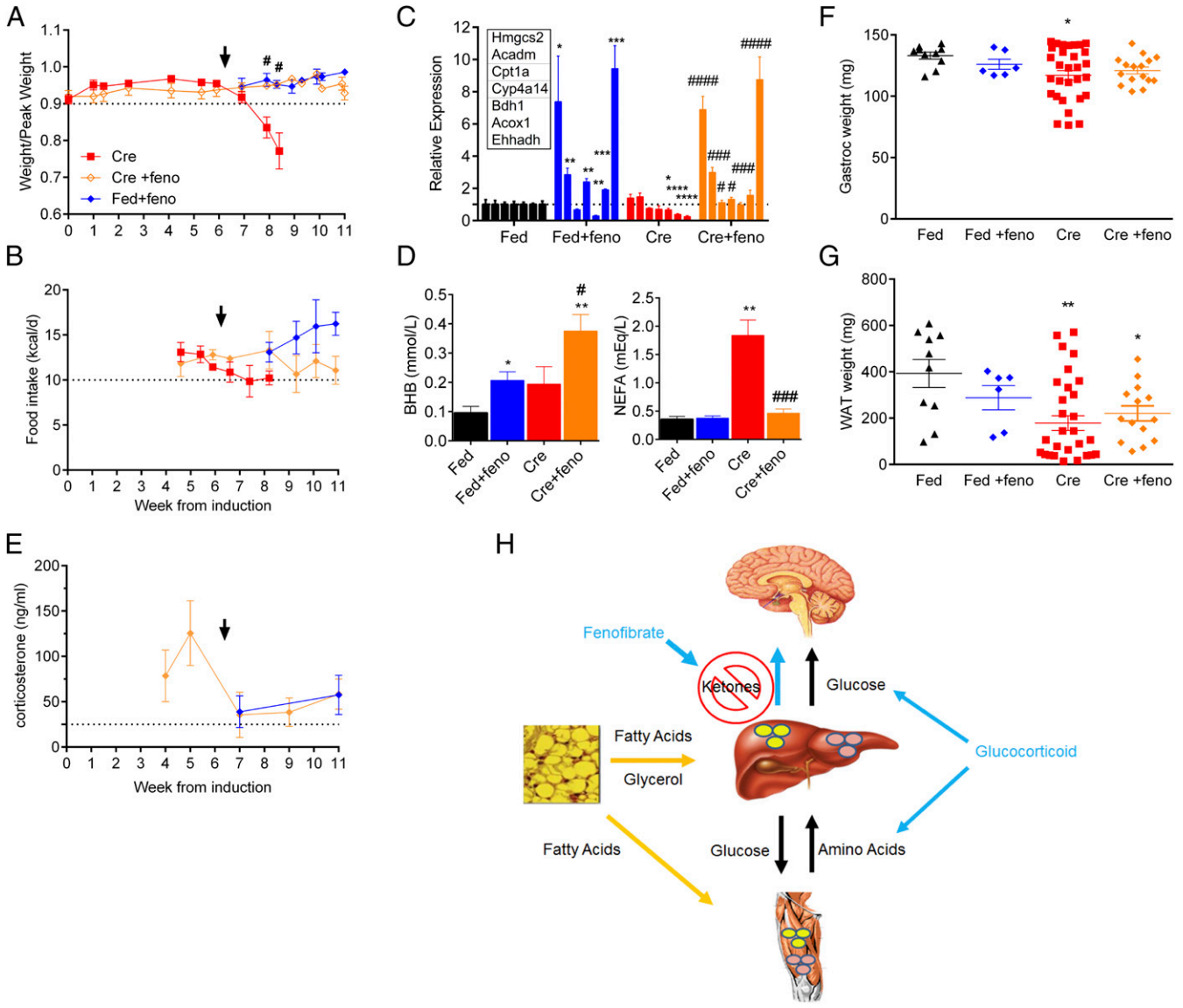

Fig. 7. Fenofibrate treatment prevents cachexia in tumor-bearing mice. (*A*) Weight normalized to peak weight over time following induction of lung cancer using adenovirus to deliver Cre recombinase in mice fed dietary fenofibrate (Cre+feno, orange open diamonds, $n = 7$) starting at 6.5 wk (black arrow) compared with Cre-treated (Cre) mice fed normal chow ($n = 20$) and nontumor bearing mice fed dietary fenofibrate (Fed+feno, blue closed diamonds, $n = 4$). (*B*) Food intake in mice from *A*. Red boxes represent Cre data reproduced from Fig. 1*B*. (*C*) Relative expression of PPARα target genes using qPCR from livers of nontumor-bearing (Fed, black bars, $n = 5$) and tumor bearing (Cre, $n = 10$) mice on a normal chow diet compared with nontumor bearing (Fed+feno, blue bars, $n = 3$) and tumor-bearing (Cre+feno, orange bars, $n = 7$) mice fed dietary fenofibrate (feno). (*D*) Serum BHB (*Left*) and NEFA (*Right*) from mice described in *C*. (*E*) Serum corticosterone levels over time following induction of lung cancer in nontumor-bearing (Fed+feno, blue diamonds, $n = 4$) and tumor-bearing (Cre+feno, orange diamonds, $n = 7$) mice fed dietary fenofibrate starting at 6.5 wk. (*F*) Gastrocnemius (Gastroc) weight from nontumor-bearing (Fed, black triangles, $n = 5$) and tumor bearing (Cre, red boxes, $n = 16$) mice on a normal chow diet compared with nontumor-bearing (Fed+feno, blue diamonds, $n = 3$) and tumor-bearing (Cre+feno, orange diamonds, $n = 7$) mice fed dietary fenofibrate (feno). (*G*) Gonadal WAT from mice described in *F*. (*H*) Changes in intermediary metabolism following onset of cachexia: excess lipolysis in adipose tissue increases serum NEFA, which can be used by the liver and skeletal muscle. Defects in hepatic ketogenesis reduce serum ketone levels resulting in excess glucocorticoid production. Glucocorticoids modulate hepatic metabolism and induce skeletal muscle degradation to enhance gluconeogenesis. Fenofibrate restores hepatic ketogenesis and reduces serum glucocorticoids thereby preventing skeletal muscle degradation. Bar graphs are mean ± SEM. Student's *t* test compared with Fed mice: $^{*}P < 0.05$, $^{**}P < 0.01$, $^{***}P < 0.001$, $^{****}P < 0.0001$. Student's *t* test compared with Cre mice: $^{\#}P < 0.05$, $^{\#\#}P < 0.01$, $^{\#\#\#}P < 0.001$, $^{\#\#\#\#}P < 0.0001$.

the relevance of our findings in samples from patients with metastatic KRAS-mutant lung cancer with or without CACS.

Methods

Animal Care and Tumor Induction. $Kras^{G12D/+}$;$Lkb1^{f/f}$ mice have been previously described (46). Mice were housed in a 12-h light/dark cycle and 22 °C ambient temperature, and received rodent chow (PicoLab Rodent 20 5053; Lab Diet) with or without fenofibrate [0.2% (wt/wt)] (68) and free access to drinking water. Adenovirus CMV-Cre (Ad5CMV-Cre) and Empty vector control were purchased from the University of Iowa Gene Transfer Vector Core (Iowa City, IA). Tumors were induced in adult (12- to 20-wk-old) male mice via intranasal administration of 75 μL of PBS containing 2.5×10^7 pfu of adenovirus and 1 mM $CaCl_2$.

Tissue Collection. Before tissues and serum collection, mice were food-deprived for 3 h in tumor-bearing mice, 18 h in fasted mice, and fasted overnight (roughly 15 h) and then allowed free access to food for 4 h in fed mice. Tail glucose was measured using a glucose meter (Ascensia) before CO_2 asphyxiation. Immediately following killing, whole blood was collected via cardiac puncture and placed immediately on ice. Next, the whole liver was

removed, weighed, and frozen in liquid nitrogen (in under 30 s). The gonadal adipose depot, kidney, and skeletal muscles (gastrocnemius, tibialis anterior) were dissected, weighed, and flash-frozen in liquid nitrogen. The EDL and soleus were dissected, pinned to a circular piece of cork board at the native muscle length, and flash-frozen in isopentane cooled liquid nitrogen. All tissues were subsequently stored at −80 °C until further processing. Lung tissue was fixed for 12 h in 4% buffered paraformaldehyde (Affymetrix) at 4 °C on a shaker, then stored in 70% ethanol at 4 °C.

Serum and Tissue Metabolites. Blood was centrifuged (10,000 × *g* for 10 min at 4 °C), and plasma was stored at −20 °C. Plasma β-hydroxybutyrate, TG (Stanbio Laboratory), NEFA (Wako Life Sciences), lactate (Sigma-Aldrich), and acetoacetate (Abcam) were determined using commercially available kits. Serum insulin, IGF1, IL-6, corticosterone (APLCO Diagnostics), and IGFBP3 (R&D Systems) levels were quantified by ELISA.

For glycogen measurements, liver tissue (30–50 mg) and dilutions of glycogen type III obtained from rabbit liver (Sigma-Aldrich) were homogenized in 0.03 N HCl. An aliquot of the homogenate was mixed with 1.25 N HCl and heated for 1 h at 95 °C. Samples were centrifuged at 18,400 × *g*, and 10 μL of supernatant was mixed with 1 mL of glucose oxidase reagent (Stanbio Laboratory). After a short incubation at 37 °C, the absorbance was read at 505 nm.

Metabolites were extracted from liver (30–50 mg) and gastrocnemius (whole muscle) using 80% methanol (69). Targeted LC/MS analyses were performed on a Q Exactive Orbitrap mass spectrometer (Thermo Scientific) coupled to a Vanquish UPLC system (Thermo Scientific). The Q Exactive operated in polarity-switching mode. A Sequant ZIC-HILIC column (2.1 mm i.d. × 150 mm, Merck) was used for separation of metabolites. Flow rate was 150 μL/min. Buffers consisted of 100% acetonitrile for A, and 0.1% NH_4OH/20 mM CH_3COONH_4 in water for B. Gradient ran from 85 to 30% A in 20 min followed by a wash with 30% A and reequilibration at 85% A. Metabolites were identified on the basis of exact mass within 5 ppm and standard retention times. Relative metabolite quantitation was performed based on peak area for each metabolite. All data analyses were done using scripts written in house.

RNA Seq and qPCR. Total RNA was extracted from liver (30–50 mg) and gastrocnemius (whole muscle) using TRIzol (Thermo Fisher) followed by clean-up using RNeasy kit (Qiagen). One microgram of total RNA of each sample was submitted to the WCM Genomics Resources Core Facility. Raw sequenced reads were aligned to the mouse reference GRCm38 using STAR (v2.4.1d, 2-pass mode) aligner. Aligned reads were quantified using Cufflinks (v2.2.1) to obtain fragments per kilobase per million (FPKM) and raw counts using HTSeq (v0.6.1) (70, 71). The computational pipelines were managed with Nextflow (72). Statistical analyses on the normalized expression values (FPKM) were performed using the Qlucore Omics Explorer 3.0 software (Qlucore). The identification of significantly differential variables between the subgroups of mRNA expression was performed using DESeq2 (v1.14.1), and variables with adjusted *P* values below 0.05 and log-transformed fold-change greater than 1 were considered significant. Differentially expressed gene symbols were imported into DAVID functional annotation tool (https://david.ncifcrf.gov/summary.jsp) to identify significantly enriched KEGG pathways. Hierarchical cluster analysis of differentially expressed mRNA was performed using the Qlucore Omics explorer. These data were uploaded to the Gene Expression Omnibus repository (GSE107470).

For qPCR, cDNA was synthesized from total RNA extracted above using SuperScript VILO Master Mix (Thermo Fisher). cDNA was amplified using the Applied Biosystems TaqMan Gene Expression Assays (Thermo Fisher) with the following primers: Acadm (Mm01323360_g1), Acox1 (Mm01246834_m1), Actb (Mm00607939_s1), Bdh1 (Mm00558330_m1), Cpt1a (Mm01231183_m1), Cyp4a14 (Mm00484135_m1), Ddit4 (Mm00512504_g1), Ehhadh (Mm00619685_m1), Hmgcs2 (Mm00550050_m1), Pik3ca (Mm00435673_m1), Pik3r1 (Mm01282781_m1), Sesn1 (Mm01185732_m1).

Histology. Lung tissues were fixed with 4% paraformaldehyde solution in PBS (Affimetrix) and were embedded into paraffin. Three-micrometer sections were cut for staining with H&E, elastica-van-gieson and Alcian blue–perodic acid Schiff (PAS). Tumor subtypes and surface area for invasive and in situ components were assessed by a blinded pathologist. In situ cancer areas were confirmed by using elastica-van-gieson staining. For goblet cells to confirm the mucinous subtype, we used Alcian blue–PAS staining.

For EDL and soleus fiber analysis, serial frozen sections (8 μm) were cut at midbelly of the muscles using a cryostat at −21 °C and placed onto glass slides (Superfrost/Plus; Fisher Scientific). Single-fiber CSA and distribution were determined in images from tissue sections immunostained for laminin, as previously described (73). Photomicrographs were taken and morphometric measurements were made with Photoshop CS3 (Adobe) using a 0.3 μm per pixel scale. Fiber data for all animals in each group were merged to create a histogram or summarized by mean and SE using Prism 6 (GraphPad). Type I, IIa, IIx, and IIb fibers were distinguished through immunohistochemistry as previously described (74) and quantified in Photoshop.

Western Blots and Antibodies. Liver (50–70 mg) and tibialis anterior (whole muscle) were lysed using lysis buffer containing 50 mM Tris·HCl (pH 7.4), 150 mM NaCl, 1 mM EDTA, 10% glycerol, 1% Nonidet P-40, 0.5% Triton X-100, and 1 tablet (per 10 mL) of protease and phosphatase inhibitor. Protein extracts (50 μg) were separated by 4–12% NuPAGE Bis-Tris gel (Invitrogen) and transferred to 0.45-μm PVDF membranes with wet transfer cells (Bio-Rad Laboratories). After 1 h of blocking with Tris-buffered saline with 0.1% (vol/vol) Tween 20 containing 5% (wt/vol) BSA, membranes were incubated overnight at 4 °C with antibodies against ACOX1 (ab184032), HMGCS2 (ab137043), BDH1 (Proteintech 15417–1-AP), p110α (BD 611399), p85 (CST 4292), Ser473 AKT (CST 4058), AKT (CST 9272), Ser2448 mTOR (CST 5536), mTOR (CST 2983), Ser792 Raptor (CST 2083), Raptor (CST 2280), Ser235/6 S6 (CST 2211), S6 (CST 2217), Ser757 ULK1 (CST 6888), Ser555 ULK1 (CST 5869), ULK1 (Sigma 7481), Thr37/46 4E-BP1 (CST 2855), 4E-BP1 (CST 9452), Ser79 ACC (CST 3661), ACC (CST 3676), Thr175 AMPK (CST 2535), AMPK (CST 2532), acetyl-Histone H3 (Lys9/Lys14) (CST 9677), GAPDH (Proteintech 10494-1-AP), and β-actin (ab8227) at a 1:1,000 dilution in 5% BSA followed by a TBST wash and the appropriate secondary antibody (1:3,000) for 1 h at room temperature. The signals were detected on HyBlot CL Autoradiography Film (Denville Scientific) with SuperSignal Western Blot enhancer solution (Thermo Fisher), scanned at 600 dpi resolution, cropped with Photoshop CS3 (Adobe), and quantified using ImageJ software version 1.49v (NIH).

For PPARα immunoprecipitation, hepatic nucleic, and cytoplasm extracts were separated using NE-PER reagents (Thermo Fisher). Nuclear (200 μg) and cytoplasm (500 μg) protein lysates were precleared with control agarose resin and IgG, and then incubated overnight with 25 μg of agarose-conjugated PPAR alpha antibody (sc-398394 AC). Input (30 μg) and immunoprecipitation protein samples were mixed in NuPAGE 4× LDS buffer (Invitrogen) and separated using a 7.5% Tris-Glycine gel and transferred to a PVDF membrane as above. For PPARα detection, a polyclonal antibody was used (Thermo PA1822A).

Statistics. Data are expressed as means ± SEM. Statistical analyses for all data were performed by Student's *t* test using Prism 6 (GraphPad) or Excel 2013 (Microsoft). Statistical significance is indicated in figures using the following denotation: $*P < 0.05$, $**P < 0.01$, $***P < 0.001$, and $****P < 0.0001$.

Study Approval. All animal care and treatments were carried out in compliance with Weill Cornell Medical College Institutional Animal Care and Use Committee guidelines.

ACKNOWLEDGMENTS. This work was supported by a grant from the Lung Cancer Research Foundation.

1. Fearon K, et al. (2011) Definition and classification of cancer cachexia: An international consensus. *Lancet Oncol* 12:489–495.
2. Stene GB, et al. (2015) Changes in skeletal muscle mass during palliative chemotherapy in patients with advanced lung cancer. *Acta Oncol* 54:340–348.
3. Baracos VE, Reiman T, Mourtzakis M, Gioulbasanis I, Antoun S (2010) Body composition in patients with non-small cell lung cancer: A contemporary view of cancer cachexia with the use of computed tomography image analysis. *Am J Clin Nutr* 91(Suppl):1133S–1137S.
4. Inagaki J, Rodriguez V, Bodey GP (1974) Proceedings: Causes of death in cancer patients. *Cancer* 33:568–573.
5. Antoun S, Borget I, Lanoy E (2013) Impact of sarcopenia on the prognosis and treatment toxicities in patients diagnosed with cancer. *Curr Opin Support Palliat Care* 7:383–389.
6. Martin L, et al. (2013) Cancer cachexia in the age of obesity: Skeletal muscle depletion is a powerful prognostic factor, independent of body mass index. *J Clin Oncol* 31:1539–1547.
7. Mendell JR, Engel WK (1971) The fine structure of type II muscle fiber atrophy. *Neurology* 21:358–365.
8. Acharyya S, et al. (2005) Dystrophin glycoprotein complex dysfunction: A regulatory link between muscular dystrophy and cancer cachexia. *Cancer Cell* 8:421–432.
9. Ciciliot S, Rossi AC, Dyar KA, Blaauw B, Schiaffino S (2013) Muscle type and fiber type specificity in muscle wasting. *Int J Biochem Cell Biol* 45:2191–2199.
10. Tisdale MJ (2009) Mechanisms of cancer cachexia. *Physiol Rev* 89:381–410.
11. Zhou X, et al. (2010) Reversal of cancer cachexia and muscle wasting by ActRIIB antagonism leads to prolonged survival. *Cell* 142:531–543.
12. Roberts EW, et al. (2013) Depletion of stromal cells expressing fibroblast activation protein-α from skeletal muscle and bone marrow results in cachexia and anemia. *J Exp Med* 210:1137–1151.
13. Langstein HN, Doherty GM, Fraker DL, Buresh CM, Norton JA (1991) The roles of gamma-interferon and tumor necrosis factor alpha in an experimental rat model of cancer cachexia. *Cancer Res* 51:2302–2306.
14. Strassmann G, Fong M, Kenney JS, Jacob CO (1992) Evidence for the involvement of interleukin 6 in experimental cancer cachexia. *J Clin Invest* 89:1681–1684.

15. Costelli P, et al. (1993) Tumor necrosis factor-alpha mediates changes in tissue protein turnover in a rat cancer cachexia model. *J Clin Invest* 92:2783–2789.
16. Morley JE, Thomas DR, Wilson M-MG (2006) Cachexia: Pathophysiology and clinical relevance. *Am J Clin Nutr* 83:735–743.
17. Schwartz MW, Seeley RJ (1997) Seminars in medicine of the Beth Israel Deaconess Medical Center. Neuroendocrine responses to starvation and weight loss. *N Engl J Med* 336:1802–1811.
18. Chrousos GP (1995) The hypothalamic-pituitary-adrenal axis and immune-mediated inflammation. *N Engl J Med* 332:1351–1362.
19. Sephton SE, et al. (2013) Diurnal cortisol rhythm as a predictor of lung cancer survival. *Brain Behav Immun* 30(Suppl):S163–S170.
20. Keith BD (2008) Systematic review of the clinical effect of glucocorticoids on nonhematologic malignancy. *BMC Cancer* 8:84.
21. Chang W-P, Lin C-C (2017) Relationships of salivary cortisol and melatonin rhythms to sleep quality, emotion, and fatigue levels in patients with newly diagnosed lung cancer. *Eur J Oncol Nurs* 29:79–84.
22. Suzuki K, et al. (2015) Relationship of the urine cortisol level with the performance status of patients with lung cancer: A retrospective study. *Support Care Cancer* 23: 2129–2133.
23. Mazzoccoli G, et al. (2012) Hormone and cytokine circadian alteration in non-small cell lung cancer patients. *Int J Immunopathol Pharmacol* 25:691–702.
24. Kim KS, et al. (2012) Association of worse prognosis with an aberrant diurnal cortisol rhythm in patients with advanced lung cancer. *Chronobiol Int* 29:1109–1120.
25. Lichter I, Sirett NE (1975) Serial measurement of plasma cortisol in lung cancer. *Thorax* 30:91–94.
26. Drott C, Svaninger G, Lundholm K (1988) Increased urinary excretion of cortisol and catecholami-NES in malnourished cancer patients. *Ann Surg* 208:645–650.
27. Kuo T, Harris CA, Wang J-C (2013) Metabolic functions of glucocorticoid receptor in skeletal muscle. *Mol Cell Endocrinol* 380:79–88.
28. Braun TP, et al. (2013) Cancer- and endotoxin-induced cachexia require intact glucocorticoid signaling in skeletal muscle. *FASEB J* 27:3572–3582.
29. Wing SS, Goldberg AL (1993) Glucocorticoids activate the ATP-ubiquitin-dependent proteolytic system in skeletal muscle during fasting. *Am J Physiol* 264:E668–E676.
30. Braun TP, Marks DL (2015) The regulation of muscle mass by endogenous glucocorticoids. *Front Physiol* 6:12.
31. Wu Y, et al. (2010) REDD1 is a major target of testosterone action in preventing dexamethasone-induced muscle loss. *Endocrinology* 151:1050–1059.
32. Kumari R, Willing LB, Jefferson LS, Simpson IA, Kimball SR (2011) REDD1 (regulated in development and DNA damage response 1) expression in skeletal muscle as a surrogate biomarker of the efficiency of glucocorticoid receptor blockade. *Biochem Biophys Res Commun* 412:644–647.
33. Britto FA, et al. (2014) REDD1 deletion prevents dexamethasone-induced skeletal muscle atrophy. *Am J Physiol Endocrinol Metab* 307:E983–E993.
34. Kuo T, et al. (2012) Genome-wide analysis of glucocorticoid receptor-binding sites in myotubes identifies gene networks modulating insulin signaling. *Proc Natl Acad Sci USA* 109:11160–11165.
35. Bodine SC, et al. (2001) Identification of ubiquitin ligases required for skeletal muscle atrophy. *Science* 294:1704–1708.
36. Shimizu N, et al. (2011) Crosstalk between glucocorticoid receptor and nutritional sensor mTOR in skeletal muscle. *Cell Metab* 13:170–182.
37. Waddell DS, et al. (2008) The glucocorticoid receptor and FOXO1 synergistically activate the skeletal muscle atrophy-associated MuRF1 gene. *Am J Physiol Endocrinol Metab* 295:E785–E797.
38. Gomes MD, Lecker SH, Jagoe RT, Navon A, Goldberg AL (2001) Atrogin-1, a muscle-specific F-box protein highly expressed during muscle atrophy. *Proc Natl Acad Sci USA* 98:14440–14445.
39. Sandri M, et al. (2004) Foxo transcription factors induce the atrophy-related ubiquitin ligase atrogin-1 and cause skeletal muscle atrophy. *Cell* 117:399–412.
40. von Haehling S, Anker SD (2014) Treatment of cachexia: An overview of recent developments. *J Am Med Dir Assoc* 15:866–872.
41. Lecker SH, et al. (2004) Multiple types of skeletal muscle atrophy involve a common program of changes in gene expression. *FASEB J* 18:39–51.
42. Argilés JM, Busquets S, Stemmler B, López-Soriano FJ (2014) Cancer cachexia: Understanding the molecular basis. *Nat Rev Cancer* 14:754–762.
43. Dearden S, Stevens J, Wu Y-L, Blowers D (2013) Mutation incidence and coincidence in non small-cell lung cancer: Meta-analyses by ethnicity and histology (mutMap). *Ann Oncol* 24:2371–2376.
44. Shiono M, et al. (2016) An analysis of the relationship between metastases and cachexia in lung cancer patients. *Cancer Med* 5:2641–2648.
45. Miller A, et al. (2017) Blockade of the IL-6 trans-signalling/STAT3 axis suppresses cachexia in Kras-induced lung adenocarcinoma. *Oncogene* 36:3059–3066.
46. Ji H, et al. (2007) LKB1 modulates lung cancer differentiation and metastasis. *Nature* 448:807–810.
47. Makowski L, Hayes DN (2008) Role of LKB1 in lung cancer development. *Br J Cancer* 99:683–688.
48. Argilés JM, et al. (2011) The cachexia score (CASCO): A new tool for staging cachectic cancer patients. *J Cachexia Sarcopenia Muscle* 2:87–93.
49. Ding L, et al. (2008) Somatic mutations affect key pathways in lung adenocarcinoma. *Nature* 455:1069–1075.
50. Umemoto T, Fujiki Y (2012) Ligand-dependent nucleo-cytoplasmic shuttling of peroxisome proliferator-activated receptors, PPARα and PPARγ. *Genes Cells* 17:576–596.
51. Newman JC, Verdin E (2014) Ketone bodies as signaling metabolites. *Trends Endocrinol Metab* 25:42–52.
52. Shimazu T, et al. (2013) Suppression of oxidative stress by β-hydroxybutyrate, an endogenous histone deacetylase inhibitor. *Science* 339:211–214.
53. Snell K (1980) Muscle alanine synthesis and hepatic gluconeogenesis. *Biochem Soc Trans* 8:205–213.
54. Bloemberg D, Quadrilatero J (2012) Rapid determination of myosin heavy chain expression in rat, mouse, and human skeletal muscle using multicolor immunofluorescence analysis. *PLoS One* 7:e35273.
55. Kraja AT, et al. (2010) Fenofibrate and metabolic syndrome. *Endocr Metab Immune Disord Drug Targets* 10:138–148.
56. Zúñiga J, et al. (2011) N-3 PUFA supplementation triggers PPAR-α activation and PPAR-α/NF-κB interaction: Anti-inflammatory implications in liver ischemia-reperfusion injury. *PLoS One* 6:e28502.
57. Gogos CA, et al. (1998) Dietary omega-3 polyunsaturated fatty acids plus vitamin E restore immunodeficiency and prolong survival for severely ill patients with generalized malignancy: A randomized control trial. *Cancer* 82:395–402.
58. Masri S, et al. (2016) Lung adenocarcinoma distally rewires hepatic circadian homeostasis. *Cell* 165:896–909.
59. Flint TR, et al. (2016) Tumor-induced IL-6 reprograms host metabolism to suppress anti-tumor immunity. *Cell Metab* 24:672–684.
60. Glass CK, Ogawa S (2006) Combinatorial roles of nuclear receptors in inflammation and immunity. *Nat Rev Immunol* 6:44–55.
61. Russell ST, Tisdale MJ (2005) The role of glucocorticoids in the induction of zinc-alpha2-glycoprotein expression in adipose tissue in cancer cachexia. *Br J Cancer* 92: 876–881.
62. Rivadeneira DE, et al. (1999) Glucocorticoid blockade does not abrogate tumor-induced cachexia. *Nutr Cancer* 35:202–206.
63. Hawkins RA, Biebuyck JF (1979) Ketone bodies are selectively used by individual brain regions. *Science* 205:325–327.
64. Carneiro L, et al. (2016) Evidence for hypothalamic ketone body sensing: Impact on food intake and peripheral metabolic responses in mice. *Am J Physiol Endocrinol Metab* 310:E103–E115.
65. Mayers JR, et al. (2014) Elevation of circulating branched-chain amino acids is an early event in human pancreatic adenocarcinoma development. *Nat Med* 20:1193–1198.
66. Mayers JR, et al. (2016) Tissue of origin dictates branched-chain amino acid metabolism in mutant Kras-driven cancers. *Science* 353:1161–1165.
67. de Campos-Ferraz PL, et al. (2014) An overview of amines as nutritional supplements to counteract cancer cachexia. *J Cachexia Sarcopenia Muscle* 5:105–110.
68. Oosterveer MH, et al. (2009) Fenofibrate simultaneously induces hepatic fatty acid oxidation, synthesis, and elongation in mice. *J Biol Chem* 284:34036–34044.
69. Yuan M, Breitkopf SB, Yang X, Asara JM (2012) A positive/negative ion-switching, targeted mass spectrometry-based metabolomics platform for bodily fluids, cells, and fresh and fixed tissue. *Nat Protoc* 7:872–881.
70. Teng M, et al. (2016) A benchmark for RNA-seq quantification pipelines. *Genome Biol* 17:74.
71. Engström PG, et al.; RGASP Consortium (2013) Systematic evaluation of spliced alignment programs for RNA-seq data. *Nat Methods* 10:1185–1191.
72. Di Tommaso P, et al. (2017) Nextflow enables reproducible computational workflows. *Nat Biotechnol* 35:316–319.
73. Goncalves MD, et al. (2010) Akt deficiency attenuates muscle size and function but not the response to ActRIIB inhibition. *PLoS One* 5:e12707.
74. Bergmeister KD, et al. (2016) Automated muscle fiber type population analysis with ImageJ of whole rat muscles using rapid myosin heavy chain immunohistochemistry. *Muscle Nerve* 54:292–299.